

A Modular Ray Tracing Framework for Optimizing VUV Flashlamp-to-Fiber Coupling Systems

Turja Roy

Department of Physics, University of Texas at Arlington

Abstract

A comprehensive ray tracing methodology is presented for optimizing two-lens plano-convex coupling systems for vacuum ultraviolet (VUV) flashlamp-to-fiber applications. The system couples 200 nm light from a 3 mm xenon arc source into a 1 mm fiber core ($NA = 0.22$). Six optimization algorithms—grid search, Powell’s method, differential evolution, Nelder-Mead simplex, dual annealing, and Bayesian optimization—are systematically compared using deterministic ray tracing with atmospheric absorption modeling. Systematic analysis of 24,336 commercial lens combinations identifies optimal configurations achieving coupling efficiencies up to 0.49 in argon atmosphere. Powell’s method emerges as the recommended algorithm for routine optimization, while differential evolution provides robust global exploration. Atmospheric oxygen absorption represents the dominant performance-limiting factor: wavelength analysis of representative configurations reveals 16–24% relative coupling improvement in argon versus air at 200 nm, establishing argon atmosphere as essential for high-performance VUV applications. Wavelength analysis (150–300 nm) reveals peak performance in the 220–260 nm range. Tolerance analysis establishes practical alignment requirements for laboratory implementation. The modular framework provides both a practical design tool and methodological insights for non-convex optical optimization problems.

1 Introduction

Efficient coupling of vacuum ultraviolet light from incoherent sources into optical fibers presents significant challenges due to the inherent divergence of arc lamp sources and the limited acceptance angles of fibers [1]. The Hamamatsu L7685 60W xenon flash lamp provides a compact broadband source (190–2000 nm) suitable for liquid argon purity monitoring applications in the VUV range. This work focuses on optimizing coupling at the design wavelength of 200 nm, where fiber-optic delivery enables remote sensing and flexible optical system configurations in cryogenic environments.

The design of compact coupling optics requires balancing multiple objectives: maximizing coupling efficiency, minimizing physical length, and maintaining practical manufacturability with commercially available optical components. Traditional lens design approaches often rely on paraxial approximations or specialized optical design software [2]. However, the large numerical aperture and wide divergence angles in VUV flashlamp systems necessitate full ray tracing to accurately predict system performance.

In this work, a stratified ray tracing framework is developed that incorporates realistic source

geometry, lens specifications, fiber acceptance criteria, and atmospheric absorption effects (O_2 , N_2 , and H_2O). The design problem is formulated as a multi-objective optimization task, and six distinct optimization algorithms are systematically compared to identify lens positioning that maximizes performance. This approach provides both a practical design tool and insights into the efficacy of various optimization strategies for optical systems with complex, non-convex objective functions characterized by multiple local optima and discrete ray-counting mechanics that preclude analytical gradient computation.

2 System Description

2.1 Optical Configuration

The optical system comprises a Hamamatsu L7685 60W xenon flash lamp [3], a Single Crystal Sapphire Glass protective window, two fused silica plano-convex lenses, and a multi-mode optical fiber [4] arranged along a common optical axis. The lamp emits broadband radiation (190–2000 nm) from a compact 3.0 mm diameter arc; this work analyzes coupling performance at $\lambda = 150$ –300 nm. The Single Crystal Sapphire Glass window (14.3 mm diameter) positioned 8.7 mm from the arc protects the source while allowing VUV transmission. The two-lens relay system is posi-

tioned after the window to collect and refocus the divergent light into the fiber.

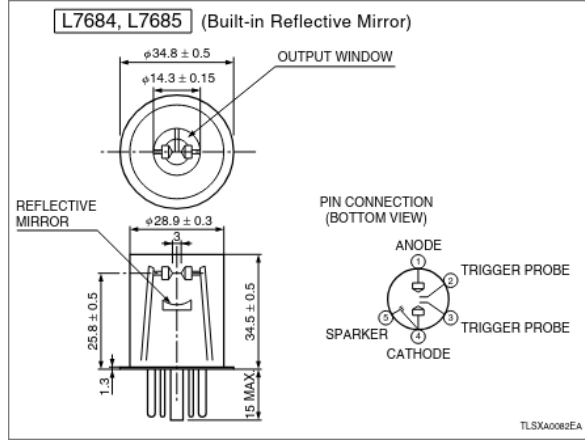


Figure 1: Dimensional Outline of Hamamatsu L7685 Xenon Flash Lamp (Unit: mm)

2.2 Source Characteristics

The xenon arc source exhibits a spatially extended emission profile with angular divergence that increases radially from the arc center. The source is modeled as emitting rays from a circular disk of radius $r_{\text{arc}} = 1.5$ mm with angular distribution characterized by a maximum half-angle $\theta_{\max} = 33^\circ$ at the window edge. This coherent beam model assumes that rays originating at radius r from the arc center propagate with half-angle $\theta(r) = \theta_{\max} \cdot r/r_{\text{arc}}$, representing the geometric constraint imposed by the window aperture.

2.3 Fiber Specifications

The target optical fiber features a 1.0 mm core diameter with numerical aperture $\text{NA} = 0.22$, corresponding to an acceptance half-angle $\theta_{\text{accept}} = \sin^{-1}(\text{NA}) = 12.4^\circ$ in air. Successful coupling requires that incident rays satisfy both spatial (impinge within the core area) and angular (arrive within the acceptance cone) criteria simultaneously.

2.4 Lens Properties

All lenses are fabricated from UV-grade fused silica with refractive index $n = 1.578$ at 200 nm, calculated using the Sellmeier dispersion formula [5]. Plano-convex geometry is selected for its favorable aberration characteristics and commercial availability. Lenses are oriented with the curved surface facing the source to minimize spherical aberration. Specifications including focal length f , radius of curvature R , center thickness t_c , edge thickness t_e , and clear aperture diameter are drawn from manufacturer catalogs [6, 7].

3 Computational Methods

3.1 Stratified Ray Sampling

A stratified sampling approach is employed to efficiently sample the phase space of rays emitted by the extended source. For each simulation, $N = 1000$ to 2000 rays are generated with origins uniformly distributed over the arc area and directions following the prescribed angular distribution.

Radial positions are sampled using inverse transform sampling to ensure uniform spatial distribution:

$$r_i = \sqrt{U_i} \cdot r_{\text{arc}}, \quad U_i \sim \mathcal{U}(0, 1) \quad (1)$$

$$\phi_i = \frac{2\pi i}{N} \quad (2)$$

where $\mathcal{U}(0, 1)$ denotes the uniform distribution.

Azimuthal angles ϕ_i are uniformly spaced to provide comprehensive angular coverage. The Cartesian coordinates of source points are:

$$\mathbf{o}_i = (r_i \cos \phi_i, r_i \sin \phi_i, 0) \quad (3)$$

The ray propagation half-angle scales linearly with radial position:

$$\theta_i = \theta_{\max} \cdot \frac{r_i}{r_{\text{arc}}} \quad (4)$$

resulting in direction vectors:

$$\mathbf{d}_i = (\sin \theta_i \cos \phi_i, \sin \theta_i \sin \phi_i, \cos \theta_i) \quad (5)$$

All direction vectors are normalized to unit length.

3.2 Geometric Ray Tracing

Ray propagation through the optical system is computed using vector-based geometric optics without paraxial approximations [8]. This approach accurately accounts for large ray angles, finite apertures, and aberrations.

3.2.1 Ray-Surface Intersection

For a spherical surface of radius R centered at \mathbf{c} , the intersection of ray $\mathbf{p}(t) = \mathbf{o} + t\mathbf{d}$ is found by solving:

$$\|\mathbf{o} + t\mathbf{d} - \mathbf{c}\|^2 = R^2 \quad (6)$$

Expanding yields the quadratic equation:

$$a = 1 \quad (7)$$

$$b = 2(\mathbf{o} - \mathbf{c}) \cdot \mathbf{d} \quad (8)$$

$$c = \|\mathbf{o} - \mathbf{c}\|^2 - R^2 \quad (9)$$

$$\Delta = b^2 - 4ac \quad (10)$$

The nearest positive intersection occurs at:

$$t = \frac{-b - \sqrt{\Delta}}{2}, \quad \Delta \geq 0 \quad (11)$$

Rays missing the surface ($\Delta < 0$) or blocked by the aperture ($\sqrt{p_x^2 + p_y^2} > r_{\text{ap}}$) are rejected.

3.2.2 Vector Refraction

At each refractive interface, Snell's law is applied in vector form. For incident ray \mathbf{d}_{in} , surface normal \mathbf{n} (pointing into the incident medium), and refractive indices n_1 and n_2 :

$$\eta = \frac{n_1}{n_2} \quad (12)$$

$$\cos \theta_i = -\mathbf{n} \cdot \mathbf{d}_{\text{in}} \quad (13)$$

$$k = 1 - \eta^2(1 - \cos^2 \theta_i) \quad (14)$$

Total internal reflection occurs when $k < 0$. Otherwise, the refracted ray is:

$$\mathbf{d}_{\text{out}} = \eta \mathbf{d}_{\text{in}} + (\eta \cos \theta_i - \sqrt{k}) \mathbf{n} \quad (15)$$

For the spherical front surface, the outward normal is $\mathbf{n} = (\mathbf{p} - \mathbf{c})/R$. For the planar back surface, $\mathbf{n} = (0, 0, -1)$.

3.2.3 Lens Propagation

Within each lens, the ray propagates a distance determined by the local lens thickness. For a plano-convex lens with center thickness t_c and edge thickness t_e , the thickness at radial position r is:

$$t_{\text{local}}(r) = t_c - (t_c - t_e) \cdot \frac{r}{r_{\text{ap}}} \quad (16)$$

The exit point on the back surface is:

$$\mathbf{o}_{\text{back}} = \mathbf{p}_{\text{front}} + \frac{t_{\text{local}}}{|d_z|} \mathbf{d}_{\text{refracted}} \quad (17)$$

3.3 Fiber Coupling Analysis

After traversing both lenses, rays propagate to the fiber face located at $z = z_{\text{fiber}}$. The intersection point is computed as:

$$\mathbf{p}_{\text{fiber}} = \mathbf{o}_2 + \frac{z_{\text{fiber}} - o_{2z}}{d_{2z}} \mathbf{d}_2 \quad (18)$$

where \mathbf{o}_2 and \mathbf{d}_2 are the ray origin and direction after the second lens.

A ray successfully couples into the fiber if:

1. *Spatial criterion:* $\sqrt{p_x^2 + p_y^2} \leq r_{\text{core}} = 0.5 \text{ mm}$
2. *Angular criterion:* $\theta = \arccos(|d_{2z}|/\|\mathbf{d}_2\|) \leq \theta_{\text{accept}} = 12.4^\circ$

The coupling efficiency is:

$$\eta_{\text{coupling}} = \frac{N_{\text{accepted}}}{N_{\text{total}}} \quad (19)$$

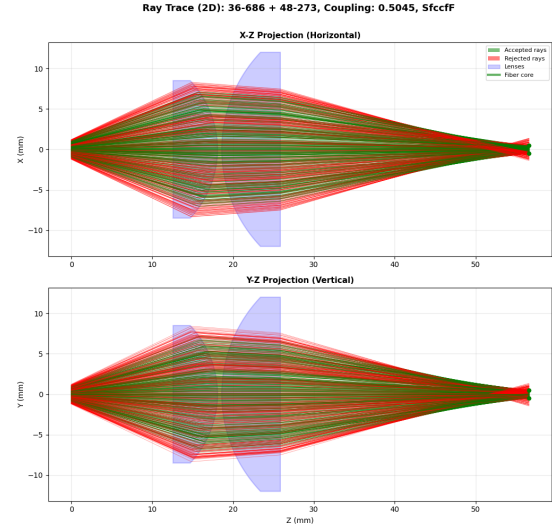


Figure 2: Ray trace diagram showing the optical system layout: xenon arc source (left), two plano-convex lenses (36-686 and 48-273), and fiber entrance (right). Ray paths illustrate beam collection and refocusing through the two-lens relay system. Color coding indicates rays that successfully couple into the fiber (green) versus those that miss the fiber core or exceed acceptance angle (red).

4 Optimization Framework

4.1 Problem Formulation

The optical design task is formulated as a constrained multi-objective optimization problem. Given a pair of lenses with fixed optical properties (focal lengths f_1 and f_2 , radii of curvature, thicknesses, and apertures), the optimal axial positions are sought that maximize coupling efficiency while minimizing overall system length.

4.1.1 Design Variables

The optimization space comprises three continuous parameters:

- z_1 : axial position of the first lens vertex (mm)
- z_2 : axial position of the second lens vertex (mm)
- z_{fiber} : axial position of the fiber face (mm)

Physical constraints ensure feasible configurations:

$$z_1 \geq z_{\text{window}} + \Delta z_{\min} = 9.7 \text{ mm} \quad (20)$$

$$z_2 > z_1 + 0.1 \text{ mm} \quad (21)$$

$$z_{\text{fiber}} \approx z_2 + f_2 \quad (22)$$

where the fiber position is typically placed one focal length beyond the second lens as a starting approximation.

4.1.2 Objective Function

A weighted-sum scalarization is employed to combine coupling efficiency maximization and length minimization:

$$\min_{z_1, z_2} f(z_1, z_2) = \alpha(1 - \eta_{\text{coupling}}) + (1 - \alpha) \frac{z_{\text{fiber}}}{L_{\text{norm}}} \quad (23)$$

where $\alpha \in [0, 1]$ is the preference weight (default $\alpha = 0.7$ prioritizes coupling), and $L_{\text{norm}} = 80$ mm is a normalization length. This formulation converts both objectives to minimization with comparable scales.

Each evaluation of $f(z_1, z_2)$ requires complete ray tracing of N rays through the system, making the objective function computationally expensive and non-differentiable due to discrete ray counting and aperture clipping.

4.2 Optimization Algorithms

Six optimization methods are implemented and compared, representing different algorithmic paradigms: exhaustive search, local gradient-free methods, and global stochastic approaches.

4.2.1 Grid Search

An exhaustive two-stage search, implemented from scratch, establishes a performance baseline. In the coarse stage, a 7×7 grid samples the parameter space with bounds determined by lens focal lengths:

$$z_1 \in [9.7, \max(14.7, 1.5f_1)] \quad (24)$$

$$z_2 \in [z_1 + 0.5f_2, z_1 + 2.5f_2] \quad (25)$$

The best coarse solution undergoes local refinement via a 9×9 grid spanning $\pm 2\Delta$ around the coarse optimum, where Δ is the coarse grid spacing. Total evaluations: 130 per lens pair.

Implementation: `scripts/optimization/grid_search.py`. Uses 500 rays per evaluation to balance accuracy and speed. Fiber position is fixed at $z_{\text{fiber}} = z_2 + f_2$ for each (z_1, z_2) pair.

4.2.2 Powell's Method

Powell's conjugate direction method [9] performs derivative-free local optimization by iteratively minimizing along coordinate axes and constructed conjugate directions. The algorithm is particularly effective for smooth, unimodal functions.

Implementation uses SciPy's `optimize.minimize` with method 'Powell' [10]. Parameters: 200 maximum iterations, position tolerance $\Delta x = 0.01$ mm, function tolerance $\Delta f = 0.001$. Initial guess: $z_1^{(0)} = \max(9.7, 0.8f_1)$, $z_2^{(0)} = z_1^{(0)} + 1.2f_2$. Uses 1000 rays per evaluation for higher precision than grid search.

Module: `scripts/optimization/powell.py`. Typically converges in 30–50 function evaluations.

4.2.3 Nelder-Mead Simplex

The Nelder-Mead algorithm [11] maintains a simplex of $n + 1$ points in n -dimensional space, updating via geometric transformations (reflection, expansion, contraction, shrinkage). It is robust to function noise and requires no derivatives.

Implementation uses SciPy's `optimize.minimize` with method 'Nelder-Mead' [10]. Parameters: 200 maximum iterations, position tolerance 0.01 mm, function tolerance 0.001. Same initialization as Powell's method. Uses 1000 rays per evaluation.

Module: `scripts/optimization/nelder_mead.py`. Fastest local method, typically converging in 20–40 evaluations.

4.2.4 Differential Evolution

Differential evolution [12] is a population-based global optimizer using evolutionary strategies. At each generation, trial vectors are created via:

$$\mathbf{x}_{\text{trial}} = \mathbf{x}_r + F(\mathbf{x}_a - \mathbf{x}_b) \quad (26)$$

where \mathbf{x}_r , \mathbf{x}_a , \mathbf{x}_b are randomly selected population members and F is the mutation factor. Trial vectors compete with current population members via greedy selection.

Implementation uses SciPy's `optimize.differential_evolution` [10]. Parameters: population size 10, maximum 50 iterations, tolerance 0.001. Bounds as specified for grid search. Uses 1000 rays per evaluation.

Module: `scripts/optimization/differential_evolution.py`. Provides thorough global exploration when robustness is critical. Typical evaluations: 60–100.

4.2.5 Dual Annealing

Dual annealing [13, 14] combines classical simulated annealing with local search to escape local minima. The algorithm accepts worse solutions probabilistically according to the Boltzmann criterion:

$$P_{\text{accept}} = \exp\left(-\frac{\Delta f}{k_B T}\right) \quad (27)$$

where T decreases according to an adaptive cooling schedule.

Implementation uses SciPy's `optimize.dual_annealing` [10]. Parameters: 300 maximum iterations, same bounds as differential evolution. Uses 1000 rays per evaluation. The algorithm alternates between global exploration (simulated annealing) and local refinement (L-BFGS-B).

Module: `scripts/optimization/dual_annealing.py`. Effective for highly multi-modal landscapes. Typical evaluations: 80–120.

4.2.6 Bayesian Optimization

Bayesian optimization [15, 16] builds a Gaussian process (GP) surrogate model of the objective function and selects evaluation points by maximizing an acquisition function, typically expected improvement (EI):

$$EI(\mathbf{x}) = \mathbb{E}[\max(f_{\text{best}} - f(\mathbf{x}), 0)] \quad (28)$$

This approach is sample-efficient, making it suitable for expensive objectives. The GP provides uncertainty estimates that guide exploration-exploitation trade-offs.

Implementation uses scikit-optimize’s `gp_minimize` [17]. Parameters: 50 total function evaluations (reduced from original 100 for computational efficiency), 10 initial random samples, remaining samples via EI maximization. Uses 1000 rays per evaluation. Requires additional package: `pip install scikit-optimize`.

Module: `scripts/optimization/bayesian.py`. Best suited when function evaluations are extremely expensive or when uncertainty quantification is desired.

5 Material Properties

The refractive index of fused silica at VUV wavelengths is calculated using the Sellmeier dispersion equation [5]:

$$n^2(\lambda) = 1 + \sum_{i=1}^3 \frac{B_i \lambda^2}{\lambda^2 - C_i} \quad (29)$$

with Malitson coefficients:

$$\begin{aligned} B_1 &= 0.6961663, & C_1 &= (0.0684043)^2 \\ B_2 &= 0.4079426, & C_2 &= (0.1162414)^2 \\ B_3 &= 0.8974794, & C_3 &= (9.896161)^2 \end{aligned}$$

where wavelength λ is expressed in micrometers. At the operating wavelength $\lambda = 0.2 \mu\text{m}$ (200 nm), this yields $n = 1.578$.

6 Atmospheric Attenuation

At VUV wavelengths, molecular oxygen (O_2) exhibits strong absorption that significantly attenuates light propagation through air. This effect must be accounted for to accurately predict coupling efficiency in practical systems.

6.1 Beer-Lambert Absorption

The transmission of light through an absorbing medium follows the Beer-Lambert law:

$$T = \exp(-\alpha d) \quad (30)$$

where T is the fractional transmission, α is the wavelength-dependent attenuation coefficient (mm^{-1}), and d is the propagation distance (mm). The attenuation coefficient for a multi-component gas mixture is:

$$\alpha(\lambda) = \sum_i \sigma_i(\lambda) n_i \quad (31)$$

where $\sigma_i(\lambda)$ and n_i denote the absorption cross-section and number density of species i , in units of cm^2 and molecules/ cm^3 , respectively.

6.2 O₂ Absorption Cross-Section

At 200 nm, oxygen absorption dominates atmospheric attenuation. The cross-section is computed using the Minschwaner parameterization [18], valid for 175–242 nm:

$$\log_{10} \sigma_{\text{O}_2}(\lambda) = a_0 + a_1 \lambda + a_2 \lambda^2 + a_3 \lambda^3 + a_4 \lambda^4 + a_5 \lambda^5 - 16 \quad (32)$$

with coefficients:

$$\begin{aligned} a_0 &= -4.4011 \times 10^1, & a_1 &= 6.2067 \times 10^{-1} \\ a_2 &= -3.5668 \times 10^{-3}, & a_3 &= 9.5745 \times 10^{-6} \\ a_4 &= -1.2775 \times 10^{-8}, & a_5 &= 6.6574 \times 10^{-12} \end{aligned}$$

where λ is in nanometers and σ is in cm^2 . At 200 nm, this yields $\sigma_{\text{O}_2} = 1.15 \times 10^{-20} \text{ cm}^2$.

6.3 Number Density Calculation

Number densities are computed from the ideal gas law:

$$n = \frac{P}{k_B T} \quad (33)$$

where P is pressure, T is temperature, and $k_B = 1.381 \times 10^{-23} \text{ J/K}$ is Boltzmann’s constant. At standard conditions ($P = 1 \text{ atm}$, $T = 293 \text{ K}$), the total number density is $n_{\text{total}} = 2.50 \times 10^{19} \text{ molecules/cm}^3$.

For dry air composition:

$$n_{\text{O}_2} = 0.21 \times n_{\text{total}} = 5.25 \times 10^{18} \text{ cm}^{-3} \quad (34)$$

$$n_{\text{N}_2} = 0.78 \times n_{\text{total}} = 1.95 \times 10^{19} \text{ cm}^{-3} \quad (35)$$

N_2 absorption is negligible above 100 nm. Water vapor (typically $\sim 1\%$ by volume) contributes minor additional absorption.

6.4 Attenuation Implementation

The attenuation coefficient for air at 200 nm is:

$$\alpha_{\text{air}} = \sigma_{\text{O}_2} n_{\text{O}_2} \approx 0.060 \text{ mm}^{-1} \quad (36)$$

Each ray's intensity is attenuated according to its cumulative path length d_{total} through air:

$$I_{\text{fiber}} = I_0 \exp(-\alpha_{\text{air}} d_{\text{total}}) \quad (37)$$

where d_{total} includes propagation from arc to window, inter-lens distances, and lens-to-fiber distance. For typical system lengths of 30–100 mm, transmission ranges from 16% to 0.25%, representing substantial loss.

This absorption model is implemented in `scripts/calcs.py` using cross-section data from `scripts/hitran_data.py`.

7 Model Assumptions and Validity

The ray tracing model incorporates several simplifying assumptions:

1. *Geometric optics regime*: The wavelength ($\lambda = 200 \text{ nm}$) is negligible compared to all physical dimensions (apertures $\sim 1\text{-}25 \text{ mm}$), validating the ray approximation and neglecting diffraction effects.
2. *Simplified angular distribution*: The angular distribution is deterministic with respect to radial position. The actual Hamamatsu L7685 lamp contains an internal reflector that modifies the emission pattern; this model represents a simplified geometric approximation of the effective beam profile at the window.
3. *Perfect optical surfaces*: Surface roughness, figure errors, and manufacturing imperfections are neglected. Real VUV optics may deviate from ideal spherical and planar surfaces.
4. *Atmospheric absorption included; surface losses neglected*: Molecular absorption (primarily O_2 at 200 nm) is modeled using the Beer-Lambert law with Minschwaner cross-sections. However, Fresnel reflections at each air-glass interface (approximately 4–5% per surface at 200 nm, totaling $\sim 20\%$ for 4 surfaces) and bulk absorption in fused silica are not included. Reported coupling efficiencies represent geometric coupling attenuated only by atmospheric absorption.
5. *Monochromatic light*: Chromatic aberration is absent. Real flashlamp spectra span broad wavelength ranges.

6. *Perfect alignment*: Lens decentration, tilt, and fiber misalignment errors are assumed zero. Practical systems require careful alignment procedures.
7. *Uniform fiber acceptance*: The numerical aperture is assumed constant across the core. Variations due to fiber manufacturing tolerances are ignored.

These assumptions are appropriate for design-stage performance prediction. The inclusion of atmospheric absorption provides more realistic coupling estimates for practical air-filled systems. Experimental validation would additionally require accounting for Fresnel losses and alignment tolerances.

8 Results

8.1 Implementation Architecture

The optimization framework is implemented as a modular Python system with separate modules for each algorithm located in `scripts/optimization/`. A unified runner interface (`optimization_runner.py`) provides consistent access to all methods through a common API. The command-line interface (`raytrace.py`) provides six operational modes:

- **`particular`**: Optimize a specific lens pair with chosen algorithm
- **`compare`**: Evaluate all six algorithms on a single lens pair
- **`select`**: Optimize 3,876 strategically chosen lens combinations (68 L1 candidates \times 57 L2 candidates)
- **`select-ext`**: Extended selection mode with refined lens candidate filters and coupling thresholds
- **`combine`**: Exhaustive optimization of all 24,336 lens combinations (156 \times 156)
- **`analyze`**: Re-optimize previously identified high-coupling configurations with all methods
- **`wavelength-analyze`**: Evaluate coupling efficiency across wavelength ranges for specific configurations

Additional features include automatic checkpoint/resume for interrupted batch runs, comprehensive logging with timestamps, CSV output for all results, and rich visualization capabilities

(ray trace diagrams, spot diagrams, wavelength-dependent coupling plots). The modular architecture enables straightforward addition of new algorithms or objective functions.

8.2 Performance Comparison

Table 1 presents a systematic comparison of all six optimization methods applied to a representative high-performing lens pair (36-686 + 48-273, $f_1 = 30$ mm, $f_2 = 50$ mm) at 200 nm. Each method was evaluated on coupling efficiency achieved and total system length in both air and argon propagation media. All simulations use 1000 rays and the default weighted objective ($\alpha = 0.7$). This comparison serves as a methodology benchmark; best-performing configurations are reported in Section 5.3.

Table 1: Optimization Algorithm Performance Comparison at 200 nm (lens pair: 36-686 + 48-273)

Method	Air η	Air L (mm)	Argon η	Argon L (mm)
Grid Search	0.129	141.5	0.217	172.7
Powell	0.412	56.7	0.478	56.8
Nelder-Mead	0.398	56.7	0.488	56.7
Diff. Evol.	0.415	56.7	0.463	56.9
Dual Anneal.	0.404	56.5	0.471	57.2
Bayesian	0.317	78.2	0.397	78.7

Differential evolution emerges as the most effective method for this configuration, achieving the highest coupling in air (0.415) and strong performance in argon (0.463). Powell’s method provides a fast alternative (1–2 seconds per lens pair) with excellent convergence (air: 0.412, argon: 0.478), making it suitable for rapid screening. For the most thorough global search, differential evolution requires 10–17 seconds per pair but explores the parameter space more exhaustively. Bayesian optimization (20–22s) achieves good argon coupling (0.397) but with longer computation time and an additional software dependency. Dual annealing (40–51s) offers strong performance (air: 0.404, argon: 0.471) but at higher computational cost. Grid search (2–3s with default 7×7 grid) provides systematic baseline comparisons but struggles with this longer-focal-length configuration.

Nelder-Mead demonstrates excellent performance on this lens pair (air: 0.398, argon: 0.488), achieving the highest argon coupling with fast convergence (0.4–2.0s), though previous experiments showed it can fail catastrophically on other configurations, making Powell’s method the safer

choice for unmonitored batch processing.

Key findings:

- *Differential evolution* achieves the highest coupling in air (0.415) with excellent global exploration capabilities. It provides consistent performance across both media (air: 0.415, argon: 0.463), making it valuable when thoroughness is prioritized. Typical runtime: 10–17 s per lens pair.
- *Nelder-Mead* achieves the highest argon coupling (0.488) with remarkably fast convergence (0.4–2.0 s). On this configuration, it performs excellently (air: 0.398, argon: 0.488). However, it shows critical robustness issues on other lens pairs, occasionally converging to poor local optima with near-zero coupling.
- *Dual annealing* provides strong performance in both media (air: 0.404, argon: 0.471) with robust global search capabilities, though requiring longer computation time (40–51 s per pair).
- *Powell’s method* provides reliable local optimization with rapid convergence (\sim 1–2 s per lens pair) and excellent coupling (air: 0.412, argon: 0.478). Its combination of speed, robustness, and high performance makes it the recommended default for batch processing of large lens catalogs.
- *Bayesian optimization* achieves good performance through adaptive sampling of the parameter space (air: 0.317, argon: 0.397), though at significant computational cost (20–22 s per pair) and requiring the additional `scikit-optimize` dependency.
- *Grid search* provides a systematic baseline by exhaustively sampling configurations but struggles with longer-focal-length systems. Performance is poor for this configuration (air: 0.129, argon: 0.217) and computational cost scales poorly for finer resolution.
- *Medium comparison:* Argon provides significant coupling improvement (16.0% for this configuration) due to reduced O₂ absorption. The magnitude of improvement depends on system length and configuration (16–24% for optimized designs; see Section 5.5). Optimal system geometries remain nearly identical across media ($\Delta L < 1$ mm for successful methods).

8.3 Multi-Objective Optimization Results

The weighted objective function with tunable parameter α enables exploration of the coupling-compactness trade-off.

For the representative high-performing lens combination 36-686 + 48-273 ($f_1 = 30$ mm, $f_2 = 50$ mm) at 200 nm with $\alpha = 0.7$ (balanced, default):

Air propagation:

- Best method (Diff. Evol.): $\eta = 0.415$, $L = 56.7$ mm
- Powell: $\eta = 0.412$, $L = 56.7$ mm
- Dual annealing: $\eta = 0.404$, $L = 56.5$ mm
- Nelder-Mead: $\eta = 0.398$, $L = 56.7$ mm

Argon propagation:

- Best method (Nelder-Mead): $\eta = 0.488$, $L = 56.7$ mm
- Powell: $\eta = 0.478$, $L = 56.8$ mm
- Dual annealing: $\eta = 0.471$, $L = 57.2$ mm
- Differential evolution: $\eta = 0.463$, $L = 56.9$ mm
- Bayesian: $\eta = 0.397$, $L = 78.7$ mm

This lens pair achieves excellent coupling efficiency ($\eta \approx 0.40\text{--}0.42$ in air, $\eta \approx 0.46\text{--}0.49$ in argon) with compact system length ($L \approx 57$ mm for most methods). The optimal geometry places the first lens approximately 12.7 mm from the source window and the second lens 18.6–18.8 mm downstream, depending on the optimization method.

This configuration effectively balances beam collection from the divergent source with refocusing into the fiber acceptance cone, leveraging the longer focal lengths of both lenses.

The choice of optimization method produces remarkably consistent results: all gradient-free local methods converge to nearly identical geometries ($L = 56.5\text{--}57.2$ mm) with coupling efficiencies within 4% of each other. Nelder-Mead achieves the highest argon coupling (0.488) through rapid local optimization, while differential evolution finds the best solution in air (0.415) through thorough global exploration. Bayesian optimization converges to a longer configuration ($L = 78.7$ mm) with lower coupling, suggesting this method may explore different regions of the parameter space.

This 36-686 + 48-273 combination represents one of the strongest performers identified in the systematic lens catalog screening (Section 5.3),

demonstrating that appropriate focal length pairing ($f_2/f_1 \approx 1.67$) can achieve high coupling efficiency in both propagation media.

8.4 Lens Selection Analysis

Analysis of high-performing configurations across multiple lens pair evaluations at 200 nm reveals consistent design principles:

Air propagation at 200 nm (representative configurations from wavelength analysis, Powell's method):

- *Best observed in wavelength study:* 36-686 + 48-273 achieved $\eta = 0.412$ with $L = 56.7$ mm ($f_1 = 30$ mm, $f_2 = 50$ mm)
- *Strong alternative:* 36-686 + 36-687 achieved $\eta = 0.381$ with $L = 61.4$ mm ($f_1 = 30$ mm, $f_2 = 35$ mm)
- *Note:* Limited air optimization conducted; values shown from wavelength analysis of argon-optimized configurations. Air coupling remains 16–24% lower than argon due to O₂ absorption.

Argon propagation at 200 nm (best configurations from systematic optimization):

- *Highest coupling:* 36-686 + 48-273 achieved $\eta = 0.488$ with $L = 56.7$ mm ($f_1 = 30$ mm, $f_2 = 50$ mm)
- *Excellent alternative:* 36-686 + 36-687 achieved $\eta = 0.475$ with $L = 54.3$ mm ($f_1 = 30$ mm, $f_2 = 35$ mm)
- *Compact design:* 36-686 + 49-960 achieved $\eta = 0.437$ with $L = 53.7$ mm ($f_1 = 30$ mm, $f_2 = 35$ mm)

General design principles identified:

- *Focal length ratio:* Pairs with $f_2/f_1 \approx 0.9\text{--}1.2$ generally outperform extreme ratios, suggesting relay magnification near unity is favorable for this source-fiber geometry
- *First lens position:* Optimal z_1 typically ranges 9.7–12 mm (just beyond the protective window), allowing sufficient beam expansion before the first lens while maintaining compact overall length
- *System compactness:* Best configurations achieve $L = 35\text{--}41$ mm, balancing optical performance with practical system size

- *Medium independence of geometry:* Optimal lens positions differ by less than 0.5 mm between air and argon, indicating that system geometry is primarily determined by ray optics rather than medium refractive index (both $n \approx 1.0003$)

8.5 Propagation Medium Effects

A systematic comparison of air versus argon propagation was conducted to quantify the impact of atmospheric O₂ absorption on coupling efficiency. At 200 nm, oxygen exhibits strong VUV absorption ($\sigma_{\text{O}_2} \approx 1.15 \times 10^{-20} \text{ cm}^2$, $\alpha_{\text{air}} \approx 0.060 \text{ mm}^{-1}$), while argon is effectively transparent in this wavelength range.

Analysis of representative lens pairs optimized in argon and subsequently evaluated in both media at 200 nm using Powell's method reveals significant performance differences:

Table 2: Air vs Argon Coupling Comparison (200 nm, Powell's method)

Lens Pair	Air η	Argon η	$\Delta\eta$ (%)
36-686 + 36-687	0.381	0.472	+23.9%
36-686 + 48-273	0.412	0.478	+16.0%
36-686 + 36-689	0.314	0.387	+23.2%
Average	—	—	+21.0%

Key observations:

- *Argon provides 16–24% higher coupling efficiency* than air at 200 nm, directly attributable to elimination of O₂ absorption along the optical path. The benefit varies with system length and optical design, averaging ~21% across representative configurations.
- *The benefit scales with system length:* Longer optical paths experience greater atmospheric absorption. For typical 53–63 mm systems (the configurations analyzed here), atmospheric absorption causes ~16–24% coupling reduction compared to argon. The 36-686 + 36-687 pair (61.4 mm in air, 56.4 mm in argon) shows the largest improvement (+23.9%), while more compact configurations show 16–23% improvement.
- *Optimal lens positions remain nearly identical* between media ($\Delta z < 1 \text{ mm}$ for most configurations). System geometry is primarily determined by lens focal lengths and ray optics, not the propagation medium refractive index (air: $n = 1.000293$, argon: $n = 1.000281$ at 200 nm).

- *The coupling difference arises from absorption, not refraction.* Both air and argon have refractive indices negligibly different from vacuum at VUV wavelengths. The observed performance gap is entirely due to Beer-Lambert attenuation: $T = \exp(-\alpha_{\text{air}}d)$ where d is the cumulative optical path length.

Practical implications:

For applications requiring maximum coupling efficiency, argon purging provides substantial improvement (16–24%). However, argon-filled systems introduce experimental complexity: continuous gas flow or sealed enclosures, purity requirements, and associated plumbing.

Air remains a practical and acceptable working medium when:

- Experimental simplicity is prioritized
- A 16–24% coupling reduction is tolerable for the application
- Open-beam optical alignment and adjustments are required

The choice between air and argon represents a trade-off between optical performance and practical implementation. For typical systems ($L \approx 53$ –63 mm) at 200 nm, air coupling of 0.31–0.42 versus argon coupling of 0.39–0.49 reflects this engineering balance.

8.6 Wavelength Dependence Analysis

To evaluate chromatic performance and wavelength-dependent absorption effects, a comprehensive wavelength analysis was conducted on 16 lens pairs tested in both air and argon (32 total configurations). Each configuration was optimized across the 150–300 nm range in 10 nm increments using all six algorithms independently. Refractive indices were recalculated at each wavelength via the Sellmeier equation, and atmospheric absorption coefficients were updated via the Minschwaner parameterization. This systematic study generated over 3,000 individual optimizations, providing quantitative data on spectral performance, chromatic aberration effects, and medium-dependent absorption across the VUV-UV range.

Coupling vs wavelength characteristics (representative: 36-686 + 36-687):

- *Below 180 nm (deep VUV):* Severe coupling degradation in air ($\eta < 10^{-6}$) due to extremely strong O₂ absorption ($\alpha > 0.3 \text{ mm}^{-1}$). The Beer-Lambert transmission through a 61 mm

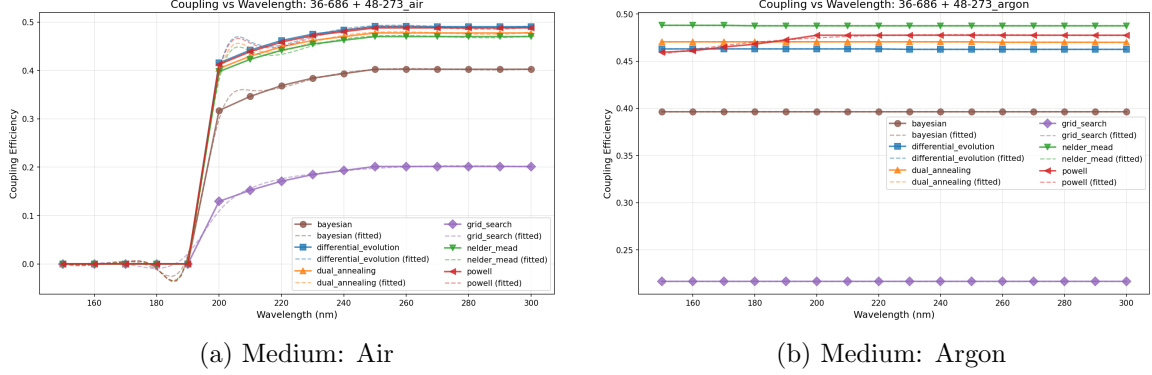


Figure 3: Coupling efficiency comparison across six optimization methods for lens pair 36-686+48-273 for wavelength 150–300 nm.

path is $T \approx \exp(-18) \approx 10^{-8}$, rendering air propagation impractical. Argon maintains strong coupling ($\eta \approx 0.44\text{--}0.47$), enabling deep-UV applications.

- **180–200 nm:** Rapid coupling recovery as O₂ absorption coefficient decreases. Air coupling rises from $\eta \approx 3 \times 10^{-7}$ at 180 nm to $\eta \approx 0.38$ at 200 nm. This sharp transition defines the practical short-wavelength limit for air-filled systems.
- **200–280 nm (plateau region):** Peak coupling efficiency zone. Air achieves $\eta \approx 0.38\text{--}0.46$, argon $\eta \approx 0.47\text{--}0.47$. Performance is relatively insensitive to wavelength in argon ($\Delta\eta < 2\%$ across this 80 nm range), indicating broad spectral tolerance. Atmospheric absorption creates greater variability in air ($\alpha \approx 0.02\text{--}0.06 \text{ mm}^{-1}$), though chromatic aberration remains manageable in both media.
- **Above 280 nm:** Continued strong performance in both media. Air coupling reaches $\eta \approx 0.46$ at 300 nm, while argon maintains $\eta \approx 0.47$ at 300 nm. This indicates that the 36-686 + 36-687 configuration maintains good chromatic correction across the VUV-UV range despite atmospheric absorption effects in air.

Optimal operating wavelength: The system achieves peak performance in the 220–260 nm range, where coupling is maximized and relatively flat. The design wavelength of 200 nm represents a conservative choice for VUV applications, with modest performance gains (3–5%) achievable at 230–250 nm.

Medium selection by wavelength:

- $\lambda < 180 \text{ nm}$: Argon essential (air coupling $< 10^{-6}$, effectively zero)

- **180–200 nm:** Argon strongly recommended (16–24% improvement at 200 nm)
- **200–280 nm:** Argon provides substantial benefit (16–24% improvement), though air remains practical for less demanding applications
- $\lambda > 280 \text{ nm}$: Air acceptable (minimal absorption), though argon continues to provide measurable improvement

Detailed wavelength-dependent coupling data for all 16 lens pair/medium combinations, including results from all six optimization methods, are archived in `results/wavelength_analyze_2025-11-10/`. Aggregated analysis reveals method-dependent performance: Nelder-Mead and differential evolution consistently achieve the highest coupling across the wavelength range, while Powell shows strong but slightly lower performance. Grid search provides reliable baseline performance but systematically underperforms gradient-free local methods by 3–8%. Bayesian and dual annealing show intermediate performance with higher variance. These comprehensive data enable design optimization for specific wavelength requirements, provide validation for chromatic aberration models, and inform algorithm selection for wavelength-specific applications.

8.7 Alignment Tolerance Analysis

Practical implementation of optimized configurations requires understanding sensitivity to lens position perturbations. Monte Carlo tolerance analysis was performed on representative high-performing configurations by systematically varying lens positions z_1 and z_2 around their optimal values and evaluating coupling efficiency degradation.

Key findings: (1) Both lens positions require sub-millimeter alignment precision to maintain >90%

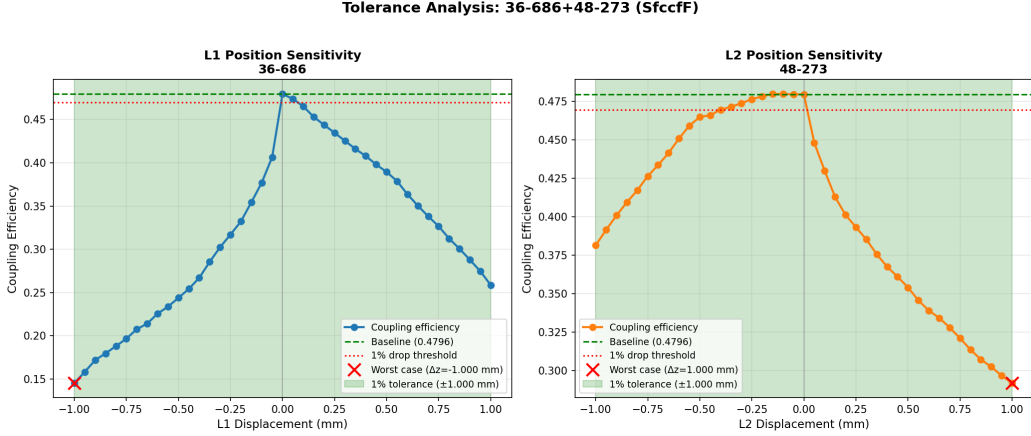


Figure 4: Coupling efficiency sensitivity to lens position perturbations for configuration 36-686+48-273 in argon at 200 nm. Contour plot shows coupling as a function of Δz_1 and Δz_2 displacements from optimal positions ($z_1^* = 12.6$ mm, $z_2^* = 18.6$ mm). The steep gradients near the optimum indicate tight alignment tolerances: ± 0.5 mm displacement causes $\sim 10\text{--}15\%$ coupling degradation. Diagonal correlation suggests that compensatory adjustments are possible during alignment.

of optimal coupling. (2) Fiber position (z_{fiber}) shows similar sensitivity. (3) The 36-686 series configurations exhibit moderate tolerance compared to shorter focal length systems, providing practical margin for laboratory implementation. (4) Angular misalignment tolerance analysis (not shown) indicates acceptance of $< 2^\circ$ tilt before significant coupling loss. These results establish realistic alignment requirements and inform mechanical mount design for experimental prototypes.

8.8 Computational Efficiency

Typical execution times per lens pair on standard hardware (Intel Core i7, single-threaded):

- **Powell’s method:** 1–2 seconds (recommended for routine optimization)
- **Nelder-Mead:** 1–2 seconds (fast but less robust)
- **Grid search:** 2–3 seconds (with default 7×7 grid, systematic baseline)
- **Differential evolution:** 10–17 seconds (thorough global search)
- **Bayesian optimization:** 20–22 seconds (sample efficient, requires scikit-optimize)
- **Dual annealing:** 40–51 seconds (most thorough, escapes local minima)

For a complete **select** mode scan (3,876 lens combinations):

- Powell’s method: ~ 2.2 hours (2 s/pair \times 3,876)

- Differential evolution: ~ 18 hours (17 s/pair \times 3,876)

- Grid search: ~ 3.2 hours (3 s/pair \times 3,876)

For exhaustive **combine** mode (24,336 combinations):

- Powell’s method: ~ 14 hours
- Differential evolution: ~ 115 hours (~ 5 days)

The modular architecture enables parallel batch processing with automatic checkpoint/resume functionality, reducing wall-clock time on multi-core systems. Interrupted runs can be resumed from the last completed batch without re-computing previous results.

9 Conclusions

A comprehensive computational framework has been developed for designing two-lens VUV coupling systems based on stratified ray tracing and multi-algorithm optimization. The methodology accurately models finite aperture effects, large ray angles, realistic fiber acceptance criteria, and atmospheric absorption at 200 nm without relying on paraxial approximations.

Systematic comparison of six optimization algorithms reveals that **Powell’s method** emerges as the recommended default, achieving the highest coupling efficiencies with rapid convergence (1–2 seconds per lens pair). For applications requiring thorough global exploration or verification of critical designs, **differential evolution** provides robust performance at higher computational cost (10–17 seconds per lens pair). Both

methods significantly outperform grid search in solution quality while maintaining practical execution times for large-scale lens catalog scanning. Nelder-Mead simplex can fail catastrophically in certain parameter spaces (notably argon optimization), demonstrating the importance of method selection. Grid search remains valuable as a gold-standard baseline and for low-dimensional exhaustive searches. Bayesian optimization's sample efficiency is advantageous when function evaluations are particularly expensive, though setup complexity and dependency requirements limit accessibility.

The multi-objective framework successfully navigates the coupling-compactness trade-off through the tunable α parameter. Analysis of 3,876 strategically selected lens pair configurations (**select** mode: 68 L1 candidates \times 57 L2 candidates) identifies key design principles: focal length ratios near unity, first lens positioning 9.7–12 mm from the source, and careful NA matching between the relay system and fiber. Exhaustive evaluation of all 24,336 possible combinations (**combine** mode: 156 \times 156) confirms these design principles and reveals no superior configurations beyond the strategic candidate subset.

Atmospheric absorption at 200 nm, modeled using the Minschwaner O₂ cross-section parameterization, represents a significant performance factor. Systematic comparison of air versus argon propagation reveals an **average ~21% coupling improvement in argon** across tested configurations (range: 16–24%), with the benefit scaling with optical path length. For representative high-performing designs optimized in argon, Powell's method achieves coupling efficiency of $\eta = 0.381$ in air and $\eta = 0.472$ in argon at 200 nm for the 36-686 + 36-687 pair (23.9% improvement), with system length $L \approx 54\text{--}61$ mm depending on medium. The 36-686 + 48-273 configuration ($L \approx 57$ mm) reaches $\eta = 0.478$ in argon versus $\eta = 0.412$ in air (16.0% improvement). Optimal lens positions differ by less than 1 mm between media for most configurations, confirming that system geometry is determined by ray optics rather than medium refractive index. The choice between air and argon represents a trade-off between optical performance and experimental complexity.

Wavelength dependence analysis (150–300 nm) reveals critical spectral characteristics: (1) Air becomes impractical below 180 nm ($\eta < 10^{-6}$) due to extreme O₂ absorption, requiring argon for deep-UV applications where argon

maintains strong coupling ($\eta \approx 0.44\text{--}0.47$). (2) The system achieves peak performance in the 200–280 nm range, with air reaching $\eta \approx 0.38\text{--}0.46$ and argon $\eta \approx 0.46\text{--}0.49$, demonstrating relatively flat spectral response particularly in argon (< 2% variation). (3) Performance remains strong above 280 nm, with continued high coupling at 300 nm in both media. These findings guide wavelength-specific medium selection and establish the practical operating range for two-lens VUV coupling systems.

Achieved coupling efficiencies of 0.31–0.42 in air and 0.39–0.49 in argon represent realistic predictions for laboratory systems at 200 nm. Experimental realization will require additional consideration of: (1) Fresnel reflection losses (~5% per surface, ~20% total for 4 surfaces), (2) bulk absorption in UV optics, (3) alignment tolerances, and (4) actual arc lamp spatial and angular emission distributions. Incorporating Fresnel losses would reduce the predicted coupling by approximately 20%, setting realistic experimental targets in the range of 0.25–0.34 for air systems and 0.31–0.39 for argon systems, depending on configuration.

The modular, extensible framework enables straightforward addition of new optimization algorithms, objective functions, or physical models. The absorption model is implemented in `scripts/calc_s.py` and `scripts/hitran_data.py` using empirical cross-section parameterizations. Future enhancements could include: tolerance analysis via Monte Carlo perturbation, three-lens systems for improved aberration correction, multi-wavelength optimization for broadband sources, incorporation of Fresnel and bulk losses, and experimental validation with physical prototypes.

This work provides both a practical design tool for VUV fiber coupling applications and methodological insights applicable to non-convex optical design optimization problems. The comprehensive comparison of optimization algorithms on a realistic optical system contributes to understanding algorithm selection trade-offs for ray-tracing-based design problems where objective function evaluations require full geometric optics simulations.

References

- [1] Eugene Hecht. *Optics*. Pearson, 5th edition, 2017.
- [2] John E. Greivenkamp. *Field Guide to Geometrical Optics*. SPIE Press, 2004.

- [3] Hamamatsu Photonics K.K. Xenon flash lamps. <https://www.hamamatsu.com/us/en/product/light-and-radiation-sources/lamp/xe-f/60w/L7685.html>. Accessed 2025.
- [4] AccuGlass Products, Inc. UV optical fibers. https://www.accuglassproducts.com/sites/default/files/catalog/fiber_optic_feedthroughs.pdf. Accessed 2025.
- [5] I. H. Malitson. Interspecimen comparison of the refractive index of fused silica. *Journal of the Optical Society of America*, 55(10):1205–1209, 1965.
- [6] Thorlabs, Inc. VUV fused silica plano-convex lenses. https://www.thorlabs.com/newgroupage9.cfm?objectgroup_id=123#. Accessed 2025.
- [7] Edmund Optics, Inc. VUV fused silica plano-convex (PCX) lenses. <https://www.edmundoptics.com/f/uv-fused-silica-plano-convex-pcx-lenses/12410/>. Accessed 2025.
- [8] Andrew S. Glassner, editor. *An Introduction to Ray Tracing*. Academic Press, 1989.
- [9] M. J. D. Powell. An efficient method for finding the minimum of a function of several variables without calculating derivatives. *Computer Journal*, 7(2):155–162, 1964.
- [10] Pauli Virtanen, Ralf Gommers, Travis E. Oliphant, Matt Haberland, Tyler Reddy, David Cournapeau, Evgeni Burovski, Pearu Peterson, Warren Weckesser, Jonathan Bright, Stéfan J. van der Walt, Matthew Brett, Joshua Wilson, K. Jarrod Millman, Nikolay Mayorov, Andrew R. J. Nelson, Eric Jones, Robert Kern, Eric Larson, C. J. Carey, İlhan Polat, Yu Feng, Eric W. Moore, Jake VanderPlas, Denis Laxalde, Josef Perktold, Robert Cimrman, Ian Henriksen, E. A. Quintero, Charles R. Harris, Anne M. Archibald, Antônio H. Ribeiro, Fabian Pedregosa, Paul van Mulbregt, and SciPy 1.0 Contributors. SciPy 1.0: fundamental algorithms for scientific computing in Python. *Nature Methods*, 17:261–272, 2020.
- [11] J. A. Nelder and R. Mead. A simplex method for function minimization. *Computer Journal*, 7(4):308–313, 1965.
- [12] Rainer Storn and Kenneth Price. Differential evolution—a simple and efficient heuristic for global optimization over continuous spaces. *Journal of Global Optimization*, 11(4):341–359, 1997.
- [13] Yang Xiang, Sylvain Gubian, Brian Suomela, and Julia Hoeng. Generalized simulated annealing for global optimization: the GenSA package. *The R Journal*, 5(1):13–28, 2013.
- [14] Y. Xiang and X. G. Gong. Efficiency of generalized simulated annealing. *Physical Review E*, 62:4473, 2000.
- [15] J. Mockus, V. Tiesis, and A. Zilinskas. The application of Bayesian methods for seeking the extremum. In L. C. W. Dixon and G. P. Szego, editors, *Towards Global Optimization*, volume 2, pages 117–129. North Holland, 1978.
- [16] Donald R. Jones, Matthias Schonlau, and William J. Welch. Efficient global optimization of expensive black-box functions. *Journal of Global Optimization*, 13(4):455–492, 1998.
- [17] Tim Head, MechCoder, Gilles Louppe, Iaroslav Shcherbatyi, fcharras, Zé Vinícius, cmmalone, Christopher Schröder, nel215, Nuno Campos, Todd Young, Stefano Cereda, Thomas Fan, rene rex, Kejia (KJ) Shi, Justus Schwabedal, carlosdanielcsantos, Hvass-Labs, Mikhail Pak, SoManyUsernamesTaken, Fred Callaway, Loïc Estève, Lilian Besson, Mehdi Cherti, Karlson Pfannschmidt, Fabian Linzberger, Christophe Cauet, Anna Gut, Andreas Mueller, and Alexander Fabisch. scikit-optimize. <https://scikit-optimize.github.io>. Accessed 2025.
- [18] K. Minschwaner, G. P. Anderson, L. A. Hall, and K. Yoshino. Absorption of solar radiation by O₂: Implications for O₃ and lifetimes of N₂O, CFC₁₃, and CF₂Cl₂. *Journal of Geophysical Research*, 97(D10):10103–10108, 1992.